PNAS RESEARCH ARTICLE | CHEMISTRY

A completely precious metal–free alkaline fuel cell with enhanced performance using a carbon-coated nickel anode

Yunfei Gao[a,1,2], Yao Yang[b,1,3], Roberto Schimmenti[c,4], Ellen Murray[c], Hanqing Peng[a], Yingming Wang[a], Chuangxin Ge[a,d], Wenyong Jiang[a], Gongwei Wang[a], Francis J. DiSalvo[b], David A. Muller[e,f], Manos Mavrikakis[c], Li Xiao[a,5], Héctor D. Abruña[b,5], and Lin Zhuang[a,d,5]

Contributed by Héctor D. Abruña; received November 3, 2021; accepted February 16, 2022; reviewed by Shane Ardo, Plamen Atanassov, and Marc Koper

Alkaline fuel cells enable the use of earth-abundant elements to replace Pt but are hindered by the sluggish kinetics of the hydrogen oxidation reaction (HOR) in alkaline media. Precious metal–free HOR electrocatalysts need to overcome two major challenges: their low intrinsic activity from too strong a hydrogen-binding energy and poor durability due to rapid passivation from metal oxide formation. Here, we designed a Ni-based electrocatalyst with a 2-nm nitrogen-doped carbon shell (Ni@CN_x) that serves as a protection layer and significantly enhances HOR kinetics. A Ni@CN_x anode, paired with a Co−Mn spinel cathode, exhibited a record peak power density of over 200 mW/cm^2 in a completely precious metal–free alkaline membrane fuel cell. Ni@CN_x exhibited superior durability when compared to a Ni nanoparticle catalyst due to the enhanced oxidation resistance provided by the CN_x layer. Density functional theory calculations suggest that graphitic carbon layers on the surface of the Ni nanoparticles lower the H binding energy to Ni, bringing it closer to the previously predicted value for optimal HOR activity, and single Ni atoms anchored to pyridinic or pyrrolic N defects of graphene can serve as the HOR active sites. The strategy described here marks a milestone in electrocatalyst design for low-cost hydrogen fuel cells and other energy technologies with completely precious metal–free electrocatalysts.

alkaline fuel cells | nonprecious | hydrogen oxidation reaction | nickel anode | carbon coating

Significance

We present a groundbreaking advance in completely nonprecious hydrogen fuel cell technologies achieving a record power density of 200 mW/cm^2 with Ni@CN_x anode and Co−Mn cathode. The 2-nm CN_x coating weakens the O-binding energy, which effectively mitigates the undesirable surface oxidation during hydrogen oxidation reaction (HOR) polarization, leading to a stable fuel cell operation for Ni@CN_x over 100 h at 200 mA/cm^2, superior to a Ni nanoparticle counterpart. Ni@CNx exhibited a dramatically enhanced tolerance to CO relative to Pt/C, enabling the use of hydrogen gas with trace amounts of CO, critical for practical applications. The complete removal of precious metals in fuel cells lowers the catalyst cost to virtually negligible levels and marks a milestone for practical alkaline fuel cells.

As one of the most promising hydrogen fuel cell technologies, alkaline polymer electrolyte fuel cells (APEFCs) have attracted great interest due to their potential to completely eliminate the need for precious metal catalysts (1–3). Although significant progress has been made in developing nonprecious metal catalysts for the oxygen reduction reaction, with activities comparable to that of noble metal catalysts (Pt, Pd, etc.) in alkaline media (4, 5), the performance of nonprecious metal catalysts for the hydrogen oxidation reaction (HOR) is still below that of precious metal catalysts (6). Therefore, in order to replace Pt-based anode catalysts in APEFCs, it is necessary to develop high-performance and durable nonprecious metal catalysts for the HOR.

Nickel-based systems remain the most active nonprecious HOR metal catalysts with promising activity (7). However, the activity of common Ni catalysts is about two orders of magnitude lower than that of state-of-the-art Pt/C catalysts (8). Several strategies have been proposed to enhance the activity of Ni-based HOR catalysts, such as alloying with other transition metals [e.g., NiFe (9), NiCu (10, 11), and NiCoMo (12)], doping with N (13), or forming metal nitrides (14, 15). However, there are few studies that address the stability of Ni (16), especially under the operation conditions of APEFCs. It should be noted that nickel oxide species form above ∼0.2 V versus reversible hydrogen electrode (RHE), which passivates the Ni catalysts (7). This instability at high potentials significantly limits their electrochemical active window. Although nickel oxides/hydroxides have been reported to enhance HOR catalytic activity of Ni (17–20), further oxidation of Ni eventually deactivates the catalysts (16). Thus, it is pivotal to investigate the durability of Ni-based catalysts, especially during fuel cell operation.

It was recently reported that surface coating can tune the electronic structure of a metal surface and improve the stability of catalysts (21–23). Small molecules such as H_2 can access the metal surface through the surface coating, where the catalytic reactions can proceed (21). Thus, utilizing the surface coating is regarded as a promising strategy to protect Ni and other metals from oxidation while maintaining high HOR activity. In a previous study (24), we found that Ni coated with hexagonal boron nitride can improve HOR activity and stability. In this work, a Ni-based electrocatalyst with a 2-nm nitrogen-doped carbon shell (Ni@CN_x) was synthesized via facile thermal treatment (25–27). The shell was found to prevent the metal catalyst from oxidizing,

Reviewers: S.A., University of California, Irvine; P.A., University of California, Irvine; and M.K., Universiteit Leiden.

The authors declare no competing interest.

[1]Y.G. and Y.Y. contributed equally to this work.

[2]Present address: Graduate School of Human and Environmental Studies, Kyoto University, Sakyo, Kyoto 606-8501, Japan.

[3]Present address: Miller Institute, Department of Chemistry, University of California, Berkeley, CA 94720.

[4]Present address: Center for Catalysis Theory, Department of Physics, Technical University of Denmark, Lyngby 2800, Denmark.

[5]To whom correspondence may be addressed. Email: hda1@cornell.edu, lzhuang@whu.edu.cn, or chem.lily@whu.edu.cn.

This article contains supporting information online at http://www.pnas.org/lookup/suppl/doi:10.1073/pnas.2119883119/-/DCSupplemental.

Published March 21, 2022.

enhancing its durability under HOR reaction conditions. The peak power density (PPD) of APEFC using this Ni@CN_x catalyst as the anode reached 480 mW/cm^2 with a Pt/C cathode and 210 mW/cm^2 with a spinel $MnCo_2O_4$ cathode at 80 °C using pure H_2 and O_2 as reactant gases. Ni@CN_x showed a PPD of 280 mW/cm^2 using H_2 mixed with 100 ppm CO and CO_2-free air as reactant gas, which suggested a significantly better CO tolerance of Ni@CN_x relative to Pt/C.

Results

In this work, Ni@CN_x was synthesized by a facile thermal treatment employing urea and nickel acetate. The crystal structure of Ni@CN_x was investigated using aberration-corrected scanning transmission electron microscopy (STEM) at the atomic scale. Ni@CN_x exhibited an average particle size of around 45 nm (*SI Appendix*, Fig. S1). The mild particle aggregation observed is likely due to the high-temperature pyrolysis treatment. As shown in the bright-field (BF) STEM image (Fig. 1*A*), a thin shell of lighter elements that was detected on the surface. BF-STEM imaging is based on the phase contrast of electrons and is more sensitive to light elements such as carbon, while the image intensity in annular dark-field (ADF) STEM scales with the atomic number ($I \propto Z^{1.7}$) and heavier elements such as Ni ($Z = 28$) will be much brighter than C ($Z = 6$) (21) (Fig. 1*E*). The thin shell on the surface was better resolved at the atomic-scale STEM image in Fig. 1*B*. Ni@CN_x exhibited the shell (red) and core (green) regions as well as the interface (cyan). The shell showed d-spacings of 3.4 Å, a characteristic value of graphitized carbon (PDF #04–006-5764). The atomic-scale STEM image in Fig. 1*C* was selected from the particle in *SI Appendix*, Fig. S2 and showed the hexagonal symmetry of face-centered cubic (fcc) Ni on the [110] zone axis, as indicated by the hexagonal diffraction spots in the Fourier transform (Fig. 1*C*, *Inset*). Dominant facets, including (111) (2.0 Å) and (200) (1.8 Å), were resolved on the atomic-scale STEM image, which matched well with the theoretical values of 2.04 and 1.76 Å, respectively, from the crystal model on the same [110] zone axis (Fig. 1*D*). A hexagonal unit cell was composed by two nearby sides of 2.2 and 2.5 Å, which were consistent with the theoretical values of 2.17 and 2.51 Å, respectively. The aforementioned STEM imaging analysis suggested that the fcc-Ni was surrounded by a 1- to 3-nm shell of *N*-doped carbon on the surface.

In an effort to further elucidate the chemical environment of Ni@CN_x catalysts, electron energy-loss spectroscopy (EELS) under STEM mode was employed to investigate the elemental distribution and assess bonding information. The Ni-core and C-shell structure became startlingly clear (Fig. 1 *E–H*) when EELS elemental maps were extracted using Ni L_3 and C K edges (*SI Appendix*, Fig. S3). The EELS map of Ni and C in Fig. 1 *F* and *G* and the composite EELS map of Ni versus C in Fig. 1*H* suggested that the Ni in the core was surrounded by a uniform C shell on the surface. EELS line profiles were extracted from the dashed box in Fig. 1*H* and quantitatively showed the carbon shell with a thickness of 1 to 3 nm (Fig. 1*I*). Additional examples of EELS mapping analysis of other Ni@CN_x confirmed that the carbon shell uniformly covered the Ni core with a thickness of 1 to 3 nm (*SI Appendix*, Fig. S4). To gain a detailed description of the local electronic structure of Ni in the catalyst, we performed energy-loss near-edge structure (ELNES) analysis with a high energy resolution of 0.5 eV (Fig. 1*J*). ELNES serves as the fingerprint of elements and reflects the density of unfilled states (unfilled density of states) above the Fermi level (E_F), which is particularly sensitive to the local atomic environment, such as valence state, chemical bonding, and coordination environment (2, 28, 29). The ELNES of Ni exhibited the characteristic sharp $L_{3,2}$ edges of metallic Ni ($[Ar]3d^94s^1$) (Fig. 1*J*), which is consistent with the EELS reference of metallic Ni thin film (*SI Appendix*, Fig. S5*B*). The L_3 edge was located at around 853 eV ($2p^{3/2}$ to $3d^{3/2}3d^{5/2}$ transition) and had a stronger intensity than the L_2 edge located at around 871 eV ($2p^{1/2}$ to $3d^{3/2}$ transition) due to the higher transition probability. The shoulder peak at around 860 eV is due to the hybridization of the 2p and 3d orbitals of metallic Ni (30). If the metallic Ni were oxidized to NiO, the multiplet structure of NiO would emerge in the EELS spectrum (*SI Appendix*, Fig. S5) (31). The absence of a NiO signal suggested a metallic Ni in the core of the Ni@CNx catalysts. The ELNES spectra from more than five different regions confirmed the existence of metallic Ni (*SI Appendix*, Fig. S6).

Rotating disk electrodes (RDEs) were used to assess the HOR activity of Ni@CN_x catalysts. To rigorously study the impact of the shell on the catalyst durability during the HOR, we selected Ni nanoparticles (NPs) with comparable particle sizes to the Ni@CN_x catalysts (*SI Appendix*, Fig. S7). Fig. 2*A* shows the HOR polarization curves for Ni@CNx and the Ni NP counterpart. At a metal loading of 0.5 mg/cm^2, the Ni@CN_x exhibited a better stability compared to Ni NPs. Even at a potential of 0.4 V versus RHE, the Ni@CN_x exhibited clear anodic current while Ni NPs were completely inactive, with the current dropping to nearly zero. The lower HOR current density in the negative-going scan is due to the formation of a surface oxide passivation layer as shown by the dashed arrows in Fig. 2*A*. Given that the HOR occurs primarily on Ni sites, the enhanced HOR activity of Ni@CN_x relative to Ni NPs is possibly/likely due to the presence of the *N*-doped carbon shell, which tunes the electronic structure of Ni and suppresses the formation of Ni oxide at high polarization potentials. Previous studies have also suggested that the enhanced activity of Ni@CN_x catalysts compared to Ni NPs was possibly due to the coated carbon shell (32) and/or N elemental doping (14, 33). An increase of Ni@CN_x catalyst loading on the glassy carbon electrode yielded higher anodic currents (*SI Appendix*, Fig. S8).

To further investigate the role of the *N*-doped carbon shell on the performance of Ni@CN_x catalysts, the thickness of the shell was tuned by varying the mass ratio of the nickel acetate and urea precursors. The pyrolysis process of urea may have generated stable *N*−C bonds when the carbon shell was formed, which would help control the thickness of the CN_x shell (34). TEM images of Ni@CN_x with different thickness of the shells are shown in *SI Appendix*, Fig. S9. With an increasing amount of urea, the CN_x shell thickness decreased from 5 nm for Ni@CN_x-1 to 3 nm for Ni@CN_x-2 and 1 nm for Ni@CN_x-3. The X-ray diffraction (XRD) patterns and X-ray photoelectron spectroscopy (XPS) spectra (*SI Appendix*, Fig. S10) of Ni@CN_x catalysts suggested that varying the mass ratios of nickel acetate and urea did not change the structure or chemical environment of Ni. Additionally, the relative ratio of nitrogen to carbon (N/C) increased with a larger amount of urea from 1.65 to 6.84% (*SI Appendix*, Figs. S10*C* and S11). The N was incorporated in the carbon shell forming C−N bonds, which is consistent with the XPS spectrum of N 1s (*SI Appendix*, Fig. S10*C*). Additionally, no evidence of metal−N bond formation was found in the ELNES of Ni (*SI Appendix*, Fig. S5 and Fig. 1*J*), which suggests that N defects do not directly interact with the Ni electrocatalyst surface. As shown in *SI Appendix*, Fig. S12*A*, the HOR activity of Ni@CN_x-2 and Ni@CN_x-3,

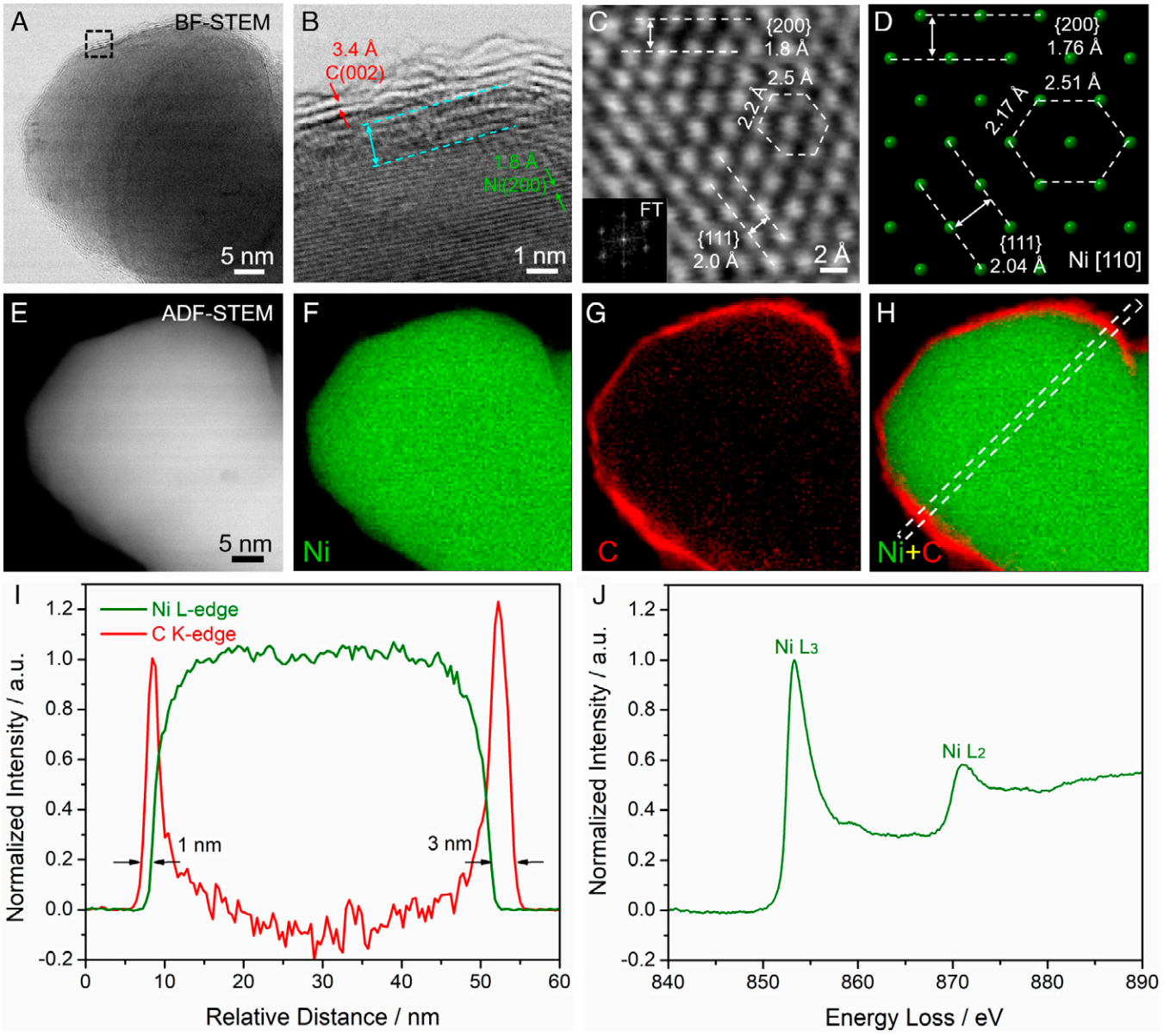

Fig. 1. Atomic-scale STEM imaging and EELS spectroscopic analysis of core-shell Ni@CN_x electrocatalysts. (*A*) BF STEM image of a Ni NP core coated with a thin carbon shell. Dashed box shows the region that is magnified in *B*. (*B*) Atomic-scale BF-STEM image of the interface between Ni (green) and C (red) as well as the 1-nm transition region (cyan). (*C* and *D*) Atomic-scale BF-STEM images of the fcc-type metallic Ni with d-spacings of {111} and {200} and hexagonal-like symmetry. The corresponding crystal model in *D* was established on the same zone axis of [110] and exhibited d-spacings and symmetry consistent with the image in *C*. *Inset* shows the diffractogram of the lattice image. (*E–H*) ADF-STEM image and EELS elemental maps of Ni (green), C (red), and the composite map of Ni versus C. (*I*) EELS line profile, extracted from the dashed box in (*H*), exhibited the carbon shell with a thickness of 1 to 3 nm. (*J*) Energy-loss near-edge structure (ELNES) of the L_3 and L_2 edges of metallic Ni at 853 and 871 eV, respectively. The shoulder peak at around 860 eV is due to the hybridization of Ni 2p and 3d orbitals. a.u., arbitrary units; FT, Fourier transform.

with thinner shells of 3 and 1 nm, respectively, increased, while their stability decreased relative to Ni@CN_x-1 with a shell of 5 nm. Ni@CN_x-2 with a medium shell thickness of 3 nm showed a good balance between HOR activity and stability. To further evaluate the stability of Ni@CN_x catalysts, the HOR currents were also characterized by chronoamperometry at different potentials (*SI Appendix*, Fig. S12*B*). With thinner shells, Ni@-CN_x-2 and Ni@CN_x-3 showed a higher current at 0.1 V and 0.2 V but lower current at 0.3 V and 0.4V, confirming the enhanced activity and slightly compromised stability relative to Ni@CN_x-1. After a series of polarizations from 0.1 to 0.4 V, the catalysts were then polarized at 0.1 V. The current values were nearly identical to the initial polarization at 0.1 V, suggesting a good stability for Ni@CN_x.

Accelerated durability tests (ADTs) were also performed to evaluate the stability of Ni@CN_x catalysts in alkaline media by performing 10,000 potential cycles between −0.1 and 0.5 V. As shown in Fig. 2*B*, Ni NPs experienced a decay of the current density at 0.05 V by about 80%; in contrast, Ni@CN_x exhibited a decay of less than 10%, indicating its significantly enhanced durability in alkaline media. Cyclic voltammetric (CV) profiles of Ni@CN_x and Ni NPs before and after ADTs are shown in *SI Appendix*, Fig. S13. While the redox current of Ni NPs experienced a severe decay, the current of Ni@CN_x was minimally affected.

The Ni@CN_x catalyst was then employed as the anode in membrane electrode assembly (MEA) measurements in an APEFC (Fig. 2*C*). With an optimal metal loading of 15 mg/cm^2,

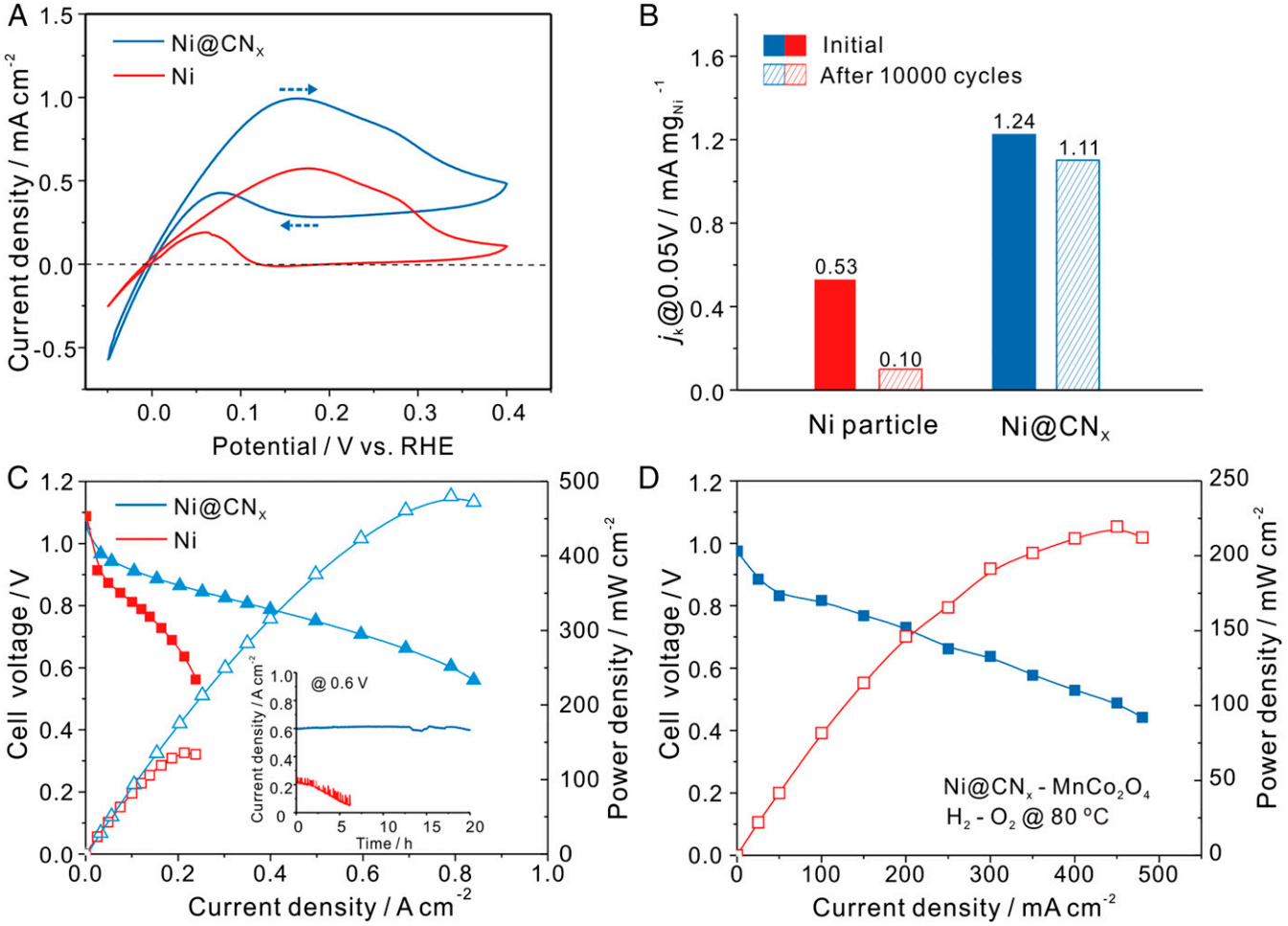

Fig. 2. The electrocatalytic performance of Ni@CN$_x$ compared with Ni NPs (Ni). (*A*) RDE profiles recorded at a rotation rate of 2,500 rpm and a scan rate of 5 mV/s. Ni@CN$_x$ electrocatalysts (blue) and Ni NPs (red). Dashed arrows reflect the positive- and negative-going directions in the CV scans. (*B*) Current density of Ni@CN$_x$ and Ni NPs measured at 0.05 V after 10,000 potential cycles from −0.1 to 0.4 V versus RHE. (*C*) Single-cell performance with anode catalysts of Ni@CN$_x$ and Ni NPs with a loading of 15 mg$_{Ni}$/cm^2 and cathode catalysts of 60 wt % Pt/C with a loading of 0.4 mg$_{Pt}$/cm^2. The *Inset* describes a stability test at a constant potential polarization at 0.6 V. (*D*) APEFC performance using Ni@CN$_x$ as anode (15 mg$_{Ni}$/cm^2) and 80 wt % $MnCo_2O_4$ (1.5 mg$_{oxide}$/cm^2) cathode catalysts. Red and blue curves represent power density and cell voltage as a function of current density, respectively. Fuel cell operation conditions in Fig. 2 *C* and *D*: cell temperature of 80 °C, gas back pressure of 0.2 MPa on both sides of the cell. Fully humidified H_2 and O_2 were fed at a flow rate of 500 mL/min. Open and closed data points in *C* and *D* represent the cell voltage and power density, respectively.

a Ni@CN$_x$ anode with a Pt/C cathode achieved a PPD of 480 mW/cm^2, while the PPD for Ni NPs was only 130 mW/cm^2. When the catalyst loadings of Ni@CN$_x$ were varied from 5 to 15 mg/cm^2, the PPD also increased from 250 mW/cm^2 to 480 mW/cm^2 (*SI Appendix*, Fig. S14). Further increases in catalyst loading did not yield a significant enhancement in the PPD, which was mainly limited by the slower mass transport and charge transfer (35). MEA performance with different back pressures, Pt loadings, and operation in synthetic air or CO_2-containing air was examined to evaluate the "practicality" of the Ni@CN$_x$ catalyst system (*SI Appendix*, Fig. S15).

Aiming for a practical APEFC, we evaluated the durability of the Ni@CN$_x$ catalyst during cell operation by applying a constant potential polarization of 0.6 V. As shown in the inset of Fig. 2*C*, the current density of Ni@CN$_x$ remained stable at about 600 mA/cm^2 for 20 h. At a constant current density of 200 mA/cm^2, Ni@CN$_x$ exhibited stable fuel cell operation for over 100 h (*SI Appendix*, Fig. S16). However, the current density of Ni NPs rapidly decreased from 200 mA/cm^2 to nearly zero within 5 h under the same test conditions. The promising durability of the Ni@CNx anode is a groundbreaking achievement for nonprecious HOR catalysts since no durable nonprecious HOR electrocatalysts operating at large current density in APEFCs have been reported before.

Aiming for completely nonprecious metal catalysts for APEFCs, we combined a Ni@CN$_x$ anode (15 mg$_{Ni}$/cm^2) with a high-loading 80 wt % $MnCo_2O_4$ (1.5 mg$_{oxide}$/cm^2) cathode, which had previously shown comparable MEA performance to a Pt/C cathode (36). As shown in Fig. 2*D*, the PPD of cell performance using a Ni-based anode and $MnCo_2O_4$ cathode achieved a record of 210 mW/cm^2. To the best of our knowledge, the MEA performance of this Ni−Mn−Co fuel cell represents the highest among alkaline fuel cells with completely precious metal–free catalysts in both the anode and cathode published to date (*SI Appendix*, Table S1). MEA performances with a Ni@CN$_x$ anode and Co−Mn cathode in realistic H_2/syn-air exhibited a PPD of ∼90 mW/cm^2 (*SI Appendix*, Fig. S17). This proof of concept with completely nonprecious MEAs, with a Ni@CNx anode and a Co−Mn cathode, lowered the catalyst cost to virtually negligible levels. While it is prudent to target fuel cell performance for high-power–density automotive applications, it is also appropriate to keep the requirements of other fuel cell markets in mind (37, 38). The Ni/Co−Mn alkaline fuel cells could pave the way for low-power–density

industrial applications, such as backup power or portable power, which prioritize low cost and longevity rather than the high-power density required for electric vehicles.

The decrease of hydrogen oxidation current at higher polarizations of Ni-based catalysts is generally ascribed to the formation of $Ni(OH)_2$ in α-form and/or β-form (39–41). Although the formation of $Ni(OH)_2$ was reported to enhance the HOR activity of Ni-based catalysts (17–19), excessive oxidation will lead to poor HOR activity and stability (13). To better understand how the shell helped improve the stability of HOR, we employed XPS to study the near-surface chemical environment of Ni after polarization at 0.1 V and 0.3 V. As shown in Fig. 3 *A–C*, after polarization at different potentials, the chemical environment of Ni changed significantly, which consisted of three components: metallic Ni, NiO, and $Ni(OH)_2$. The surface of the Ni@CN_x sample without polarization was dominated by metallic Ni, while the Ni NPs had lower metallic Ni content and more oxide/hydroxide, which indicated that the Ni@CN_x catalyst exhibited a better oxidation resistance under exposure to air. When the potential was increased from 0.1 V to 0.3 V, the relative content of metallic Ni in Ni@CN_x decreased from 63 to 28%, while the Ni NPs showed a more severe decay from 45 to 11%. When the majority of the metallic Ni was oxidized to $Ni(OH)_2$, the anodic current of Ni NPs decayed rapidly, especially at polarization potentials above 0.2 V (*SI Appendix*, Fig. S12*B*). In comparison, Ni@CN_x catalysts exhibited a better oxidation resistance at high potentials by inhibiting $Ni(OH)_2$ formation.

Additionally, the oxidation resistance through the shell of the Ni@CN_x catalyst was also detected by temperature programmed desorption (TPD) measurements. As shown in Fig. 3*D*, the peak temperature of O_{ads} desorption from the Ni@CN_x catalyst was downshifted by 37 °C compared with that on Ni NPs, which suggested that the Ni−O bond strength was weakened in the Ni@CN_x catalysts (42). A temperature programmed oxidation analysis was also used to evaluate the oxidation resistance of Ni@CN_x catalysts. As shown in *SI Appendix*, Fig. S18, the peak temperature for the formation of oxygenated chemicals was upshifted by 40 °C compared with that on Ni NPs, indicating that the CN_x shell can mitigate Ni oxidation. The tailing peak of the Ni@CN_x sample shown in Fig. 3*D* was possibly due to the decomposition of the *N*-doped carbon shell. To study the structure of the shell, nitric acid was used to etch the Ni core to obtain just the *N*-doped carbon shell, which was visualized in STEM images (*SI Appendix*, Fig. S19). The Raman spectra in *SI Appendix*, Fig. S20*A* indicated that there were a certain number of defects in the shell based on the D-to-G peak ratio to be 1.063 (23). Raman spectra of Ni@CN_x before and after acid etching showed negligible changes of the D-to-G peak ratio. This acid etching experiment suggests that mesoporous structures of the CN_x shell could allow the hydrated nickel ions to diffuse through the shell, which would also suggest that the reactants in fuel cells would be able to reach the surface of the Ni core. Additionally, according to surface area analysis (*SI Appendix*, Fig. S20*B*), the domain pore size of the pore size distribution was less than 2 nm, which provided confined channels to enhance the oxidation resistance. Finally, hydrogen TPD (H-TPD) was also used to evaluate the Ni−H bond strength, which showed that the peak temperature of H_{ads} desorption from Ni@CN_x catalysts was also downshifted by 17 °C compared to Ni NPs (*SI Appendix*, Fig. S21). This indicates that the CN_x shell could weaken the Ni−H bond strength to promote the Volmer step ($H_{ads} + OH^- = H_2O + e^-$) and thus improve the activity, which is consistent with our previous report (24).

Practical APEFCs, operating in H_2-air mode, face several challenges, including water management (2, 43, 44), carbonation of APE from air (45), and catalyst poisoning effects resulting from trace amounts of CO in H_2, which is mainly produced from steam-reforming of hydrocarbons (22). Since Pt is particularly sensitive to CO poisoning (22), a high CO tolerance is pivotal to the design of nonprecious metal anode catalysts. Here, we exposed the anode catalysts to H_2 gas with 100 ppm CO in MEA measurements. As shown in Fig. 4 *A* and *B*, the PPD of Pt/C was severely degraded in H_2 mixed with 100 ppm CO, which showed a dramatic decrease of ∼70%, from 0.71 W/cm^2 to 0.20 W/cm^2. On the other hand, Ni@CN_x exhibited a much better CO tolerance, showing a significantly smaller decay in the PPD of only ∼14%, from 0.36 W/cm^2 to 0.29 W/cm^2. Constant current polarization measurements were also conducted to evaluate the catalyst's CO tolerance. As shown in Fig. 4*C*, both Pt/C and Ni@CN_x catalysts were able to maintain a steady voltage of 0.83 V at 200 mA/cm^2. However, the voltage of Pt/C dropped to 0.45 V in H_2 mixed with

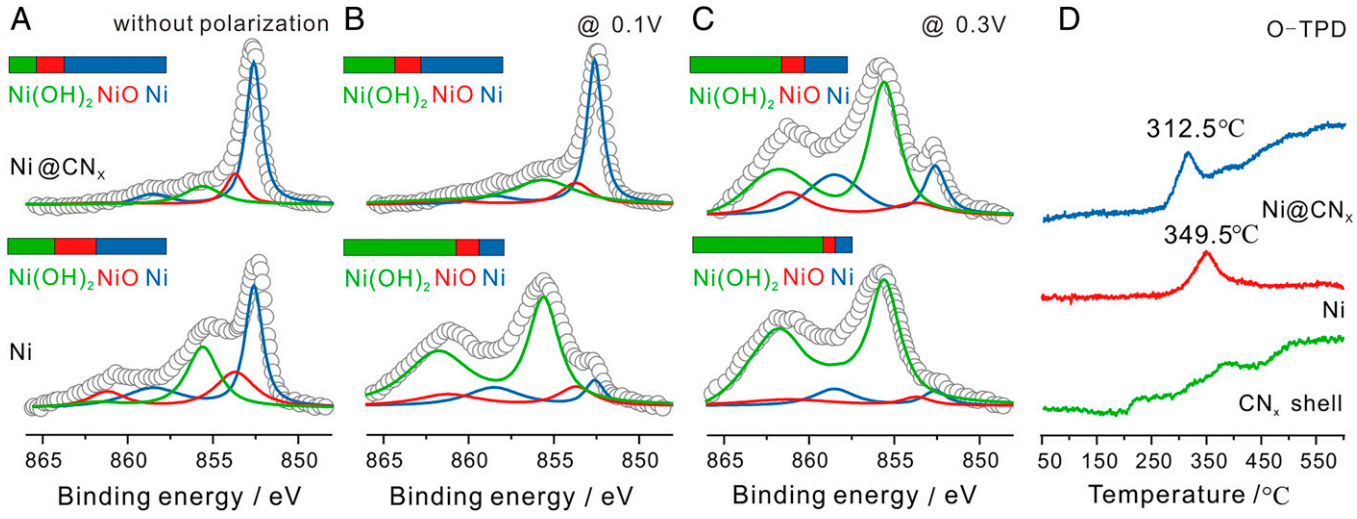

Fig. 3. XPS and TPD profiles of Ni@CN_x compared with Ni NPs. (*A–C*) XPS spectra of $Ni2p_{3/2}$ of Ni@CN_x and Ni NPs after constant potential polarization for 1 h. (*D*) TPD of oxygen adsorbed on Ni@CN_x, Ni and CN_x shell, both of which had been baked in air at 60 °C for 12 h before the test, clearly showing a weakening in the Ni−O bond strength induced by the presence of the CN_x shell.

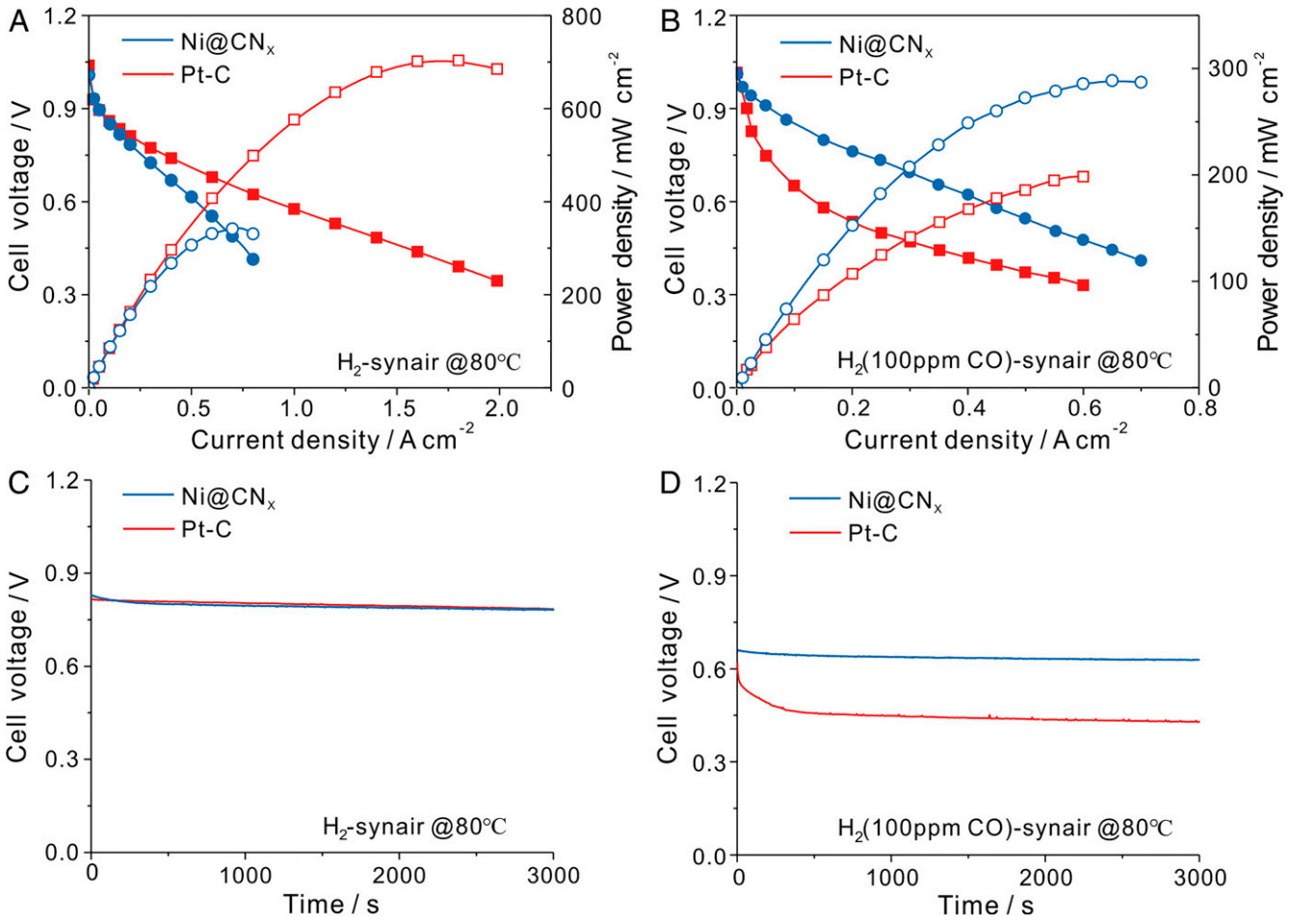

Fig. 4. The MEA performance of Ni@CN_x anode compared with Pt/C anode in pure H_2 and the addition of 100 ppm CO in APEFCs. (*A* and *B*) Cell performance with Ni@CN_x anode (15 mg/cm^2) compared with 20 wt % Pt/C (0.1 mg/cm^2), both of which used 40 wt % Pt/C as cathode with a metal loading at 0.4 mg/cm^2. The data in *A* used fully humidified pure H_2 and synthetic air (syn-air, CO_2-free) as reaction gas, while in *B*, fully humidified H_2 mixed with 100 ppm CO was used as the anode reaction gas. (*C* and *D*) Constant current polarization at 200 mA/cm^2 in both pure H_2 and H_2 with 100 ppm CO. Fuel cell operation conditions in Fig. 2 *C* and *D*: cell temperature of 80 °C, gas back pressure of 0.2 MPa on both sides of the cell. Fully humidified H_2 and air were fed at a flow rate of 500 mL/min.

100 ppm CO, while the voltage of Ni@CN_x showed a much smaller decay to 0.66 V, suggesting an impressive CO-tolerant behavior of Ni@CN_x (Fig. 4*D*). The resistance to CO poisoning is likely due to a weaker interaction strength between CO and Ni with the CN_x shell protection.

To shed light on the beneficial effects of the CN_x coating on the Ni catalysts for the HOR, we used density functional theory (DFT) calculations. In particular, we examined the effect of coating thickness and of *N*-doping at coating defects. We employed a descriptor-based analysis starting from DFT-calculated binding energies of the HOR reaction intermediates H* and OH* and of the catalyst poison O*. The binding energy of H (BE_H) has been proposed as a descriptor for HOR catalytic activity. By using DFT calculations at a comparable level of theory with respect to ours, Nørskov et al. (46) determined that the optimal HOR activity would be achieved for a BE_H that would be less stable than that of Ni(111) by 0.27 eV. Therefore, any decrease in the magnitude of BE_H on Ni(111) within that ∼0.3 eV window would be expected to lead to HOR activity improvement.

We started our analysis with a simplified model for the Ni@CN_x catalyst consisting of a monolayer of graphene supported on a Ni(111) surface in a top-fcc configuration (Ni@Graphene) (structure shown in *SI Appendix*, Fig. S22), which we determined to be the most stable structure for a graphene monolayer on Ni(111). The binding energy of the energetically most stable adsorption geometries of H*, OH*, and O* on this model are presented in Fig. 5 (numerical values for binding energies are reported in *SI Appendix*, Table S3). We note that H* and O* prefer to bind to the threefold sites of the metallic surface, whereas OH* is more stable on top of a C atom in the graphene coating, pointing away from the Ni surface. This finding suggests that the catalyst active sites for H_2 dissociation and OH* adsorption can be different in the Ni@CN_x catalyst. Furthermore, the preferential adsorption of OH* on the graphene coating could explain the enhanced durability of Ni@CN_x, as $Ni(OH)_2$ formation would be less extensive than on metallic Ni, in agreement with our XPS (Fig. 3) and CV measurements (*SI Appendix*, Fig. S13). Importantly, the binding energy of H* bound directly to Ni on a Ni(111) surface covered by one layer of graphene is −2.62 eV. Compared to a pristine Ni(111) surface (BE_H = −2.90), this reduced binding by 0.28 eV in the presence of graphene capping the Ni(111) would be sufficient to bring BE_H right around the optimal BE_H for the HOR (44). Our finding that the H* binding strength was destabilized by 0.28 eV is in qualitative agreement with the downshift in the H-TPD data shown in *SI Appendix*, Fig. S21 and can be the basis of the enhanced catalytic performance of Ni@CN_x-1 and Ni@CN_x-2 catalysts. Like H*, O* and OH* are also destabilized on Ni by the presence of

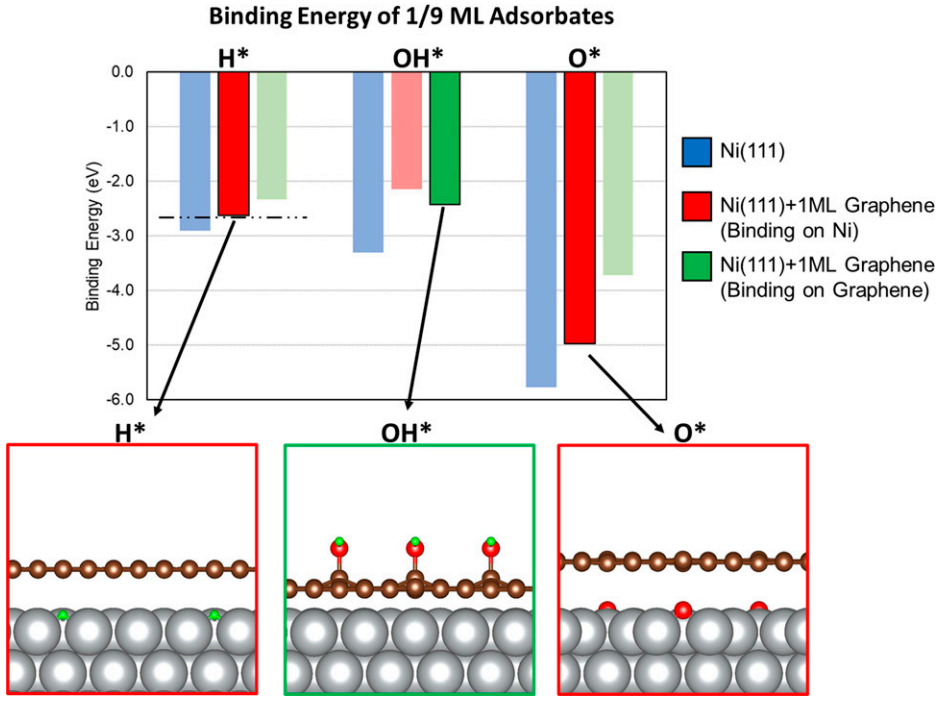

Fig. 5. Binding energy of HOR reaction intermediates H* and OH* and catalyst poison O* on pristine Ni(111) and Ni@Graphene surfaces. Blue, red, and green bars indicate the binding energy of key intermediates on a pristine Ni(111) surface, on Ni on a graphene-coated Ni(111) surface, and on top of the graphene coating, respectively. Bolded red or green bars indicate the calculated most stable H*, OH*, and O* states in the presence of the graphene-coated Ni(111). The dashed horizontal line corresponds to the HOR-optimal binding of H*. A cross-sectional view of the most stable H*, OH*, and O* geometries is shown below the chart. Ni, C, O, and H atoms are represented by silver, brown, red, and green spheres, respectively.

the graphene coating. In particular, O* bound directly to a Ni(111) surface covered by one layer of graphene was destabilized by 0.80 eV compared to pristine Ni(111), in qualitative agreement with the peak downshift observed in the oxygen TPD profile in Fig. 3*D*. Furthermore, by calculating the d-band center of Ni surface atoms in Ni(111) (−2.05 eV) and Ni@Graphene (−2.29 eV), we suggest that this negative shift of the d-band center by ∼0.25 eV (*SI Appendix*, Fig. S29) is responsible for the destabilization of all adsorbates on the Ni@Graphene model.

To elucidate the role of N defects in the CN_x coating, we performed this descriptor-based analysis on electrocatalyst models consisting of two layers of defective graphene, including pyridinic (PYR) and pyrrolic (PYL) defects, adsorbed on Ni(111). Additional details on the construction of these models are provided in the *SI Appendix*. The energy-optimized geometry of these models is shown in *SI Appendix*, Figs. S23–S25, and the respective binding energies of adsorbates on them are reported in *SI Appendix*, Tables S4–S6. These results demonstrate that irrespectively of the defect topology studied, H is either too weakly bound [PYR(3N), *SI Appendix*, Fig. S23 and PYR(4N), *SI Appendix*, Fig. S24] or too strongly bound (PYL-r, *SI Appendix*, Fig. S25) to Ni@CN_x models to explain the catalytic activity of the Ni@CN_x catalysts toward the HOR. Our analysis suggests that the presence of *N*-containing defects alone cannot explain the origin of the enhanced electrocatalytic activity of Ni@CN_x. Therefore, to explain the effect of N defects in Ni@CN_x we propose an alternative model where Ni adatoms form under reaction conditions. Remarkably, our previous studies demonstrated that *N*-doping in graphene stabilizes single-metal atom catalysts with increased activity toward water splitting and CO oxidation (47, 48).

Previous studies suggested that the synthesis of carbon-coated nickel NPs proceeds through formation of nickel carbide (Ni_3C), followed by phase segregation of carbon to the shell and nickel to the core (25, 27). However, under synthesis or reaction conditions, it is possible that trace amounts of nickel atoms may be trapped in the graphitic CN_x shell region. To determine the possible role of single-metal atoms trapped in *N*-substituted defects of graphene in the HOR, we calculated the binding energy of H*, OH*, and O* on a model Ni(111) surface coated with two layers of defective graphene in which PYR and PYL defects were saturated by a single Ni adatom. The energy-optimized geometries for these structures, without adsorbates, are shown in *SI Appendix*, Fig. S26. Numerical values for the adsorbate binding energies on these structures are shown in *SI Appendix*, Table S7, and the binding energy and optimized geometries for these structures with adsorbed OH* and O* are shown in *SI Appendix*, Figs. S27 and S28, respectively. The BE_H and the optimized structures of H* bound to supported Ni adatoms are shown in Fig. 6. The results reported in Fig. 6 corroborate the hypothesis that Ni adatoms supported on PYL (BE_H = −2.72 eV) or PYR(3N) (BE_H = −2.69 eV) defects may be the source of the increased activity toward the HOR, as they both reflect a destabilization of H* compared to H* on pristine Ni(111) by ∼0.2 eV. Interestingly, H* binds to Ni-adatom in the PYR(4N) defect much more weakly, and therefore we expect it plays no role in enhancing HOR activity in these catalysts. We noted that PYL defects, which are potentially responsible for the enhanced catalytic properties of Ni@CN_x, constitute just a minority fraction of the defects, as suggested by their DFT-calculated relative stability (*SI Appendix*, Table S2) and by the XPS characterization analysis (*SI Appendix*, Fig. S10). Thus, we propose that single Ni atoms bound to PYR (3N) graphene defects serve as one type of possible active sites of Ni@CN_x for the HOR. In closing the discussion for the nature of the active site, we noted that the measured HOR activity improvement due to graphene coating (see Fig. 2*B*) is approximately one order of magnitude, whereas

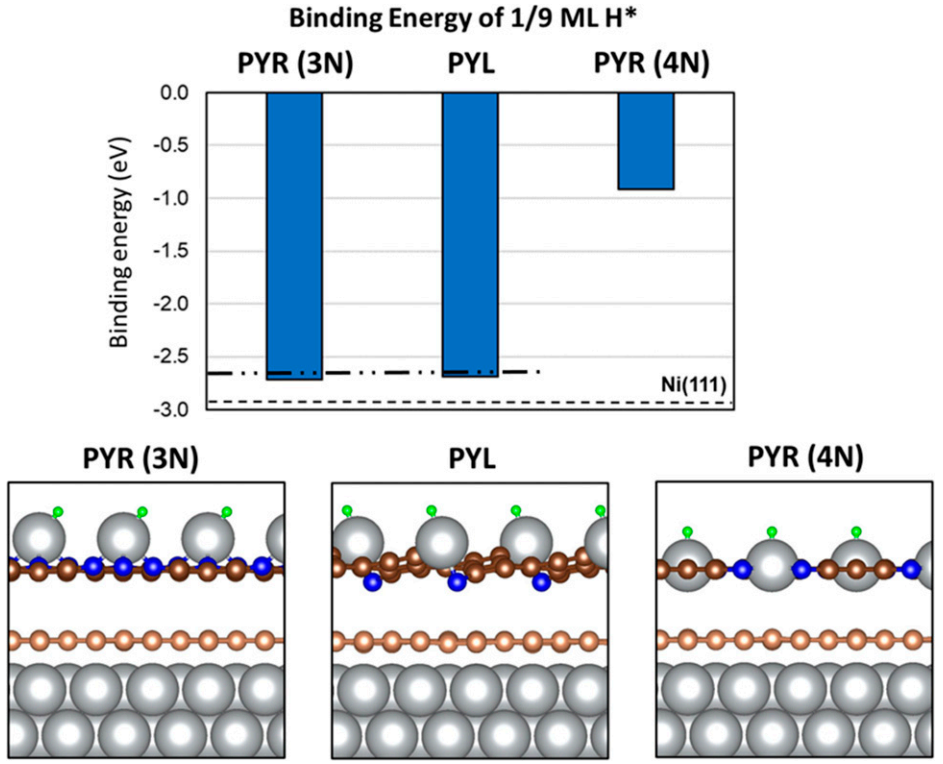

Fig. 6. Binding energy of H* on Ni@CN_x models in the presence of Ni adatoms. The dashed line on the bar chart indicates the binding energy of H* on pristine Ni(111) (−2.90 eV). The dash-dotted line corresponds to the optimal binding of H* for the HOR. A cross-sectional view of the most energetically stable geometry for H* on each Ni@CN_x model is shown below the chart. Ni, C, N, and H atoms are represented by silver, brown, blue, and green spheres, respectively. Graphene atoms in direct contact with Ni atoms in Ni@CN_x models are colored in light brown, while graphene in the second layer is colored in dark brown.

the improvement that would correspond to ∼0.3-eV destabilization of H* would be ∼4 orders of magnitude. We suggest that the less-than-ideal activity enhancement in our Ni@CN_x catalysts originates from other factors, such as O-containing defects in carbon layers (C–OH, C=O), not accounted for in our simplified models. One such factor could be the XPS-observed $Ni(OH)_2$ phase (see Fig. 3*C*) that may be adjacent to the metallic Ni phase, which would lead to a destabilization of H* by less than ∼0.3 eV, the value that corresponds to the ideal HOR catalyst. Fine-tuning our catalyst synthesis method to further reduce the presence of such factors and their influence could lead to even further improvements in HOR activity and catalyst stability.

In summary, we have developed a facile method for synthesizing stable Ni@CN_x catalysts with enhanced HOR activity and improved oxidation resistance relative to Ni NPs. The Ni@CN_x catalysts remained stable under high polarization potentials compared to Ni NPs and also showed greater durability and tolerance to CO poisoning. The in-depth STEM and EELS analysis unambiguously indicated that Ni@CN_x catalysts contained a metallic Ni core and a thin carbon shell of 1 to 3 nm. The PPD of APEFC using Ni@CN_x as an anode catalyst achieved a record value of 480 mW/cm^2 with a Pt/C cathode and 210 mW/cm^2 with a $MnCo_2O_4$/C cathode. The former represents the highest performance ever reported for a fully nonprecious fuel cell. DFT calculations and TPD measurements suggest that the CN_x shell effectively destabilized H on Ni, bringing its binding energy closer to the optimal value for HOR. In addition, the CN_x shell enhanced nickel's resistance to oxidation. Our findings highlight the strategic importance of an *N*-doped carbon shell for the synthesis of more active and durable Ni-based nonprecious anode catalysts for APEFCs.

Methods

Ni@CN_xs were prepared by a facile method using purified nickel acetate and urea as the precursors. Ni@CN_xs were characterized by XRD, XPS, Raman, and TPD measurements. The microstructures and chemical compositions were investigated by atomic-scale STEM imaging and EELS spectroscopy (Cornell Nion UltraSTEM). The HOR activity performance of Ni@CN_x was evaluated in rotating disk electrode (RDE) in 0.1 M KOH. Fuel cell performance and durability of Ni@CN_x anode were performed in MEAs with Pt/C or $MnCo_2O_4$/C cathode and QAPPTT ionomer and membrane. DFT calculations were performed using the Vienna Ab Initio Simulation Package (VASP). More experimental and computational details can be found in the *SI Appendix*.

Data Availability. All study data are included in the article and/or *SI Appendix*.

ACKNOWLEDGMENTS. This work is a collaboration between the Center for Alkaline-Based Energy Solutions (CABES), an Energy Frontier Research Center funded by the US Department of Energy (DOE), Office of Science, Basic Energy Sciences, under Grant Award No. DE-SC-0019445 and the L.Z. research group at Wuhan University, China. The synthesis of Ni@CNx, electrochemical measurements, MEA, XPS, and TPD tests were supported by the National Key Research and Development Program (Grant No. 2018YFB1502300), the National Natural Science Foundation of China (Grant Nos. 21991154, 21991150, 22122204, and 21872108), Wuhan University Innovation Team (Grant No. 2042017kf0232), and the Fundamental Research Funds for the Central Universities (Grant No. 2042019kf0270). The STEM-EELS characterization and synthesis of Co−Mn spinels at Cornell and the DFT simulation at University of Wisconsin-Madison were both supported by CABES. Y.Y. and D.A.M. acknowledge the use of STEM facilities at the Cornell Center for Materials Research, which are supported through the National Science Foundation Materials Research Science and Engineering Center) program (Grant No. DMR-1719875). The computational work was partially performed using supercomputer resources at National Energy Research Scientific Computing

Center (NERSC) and at the Center of Nanoscale Materials (CNM) at Argonne National Laboratory (ANL). NERSC and CNM/ANL are supported by the US DOE, Office of Science under Contract Nos. DE-AC02-05CH11231 and DE-AC02-06CH11357, respectively.

Author affiliations: [a]College of Chemistry and Molecular Sciences, Hubei Key Lab of Electrochemical Power Sources, Wuhan University, Wuhan 430072, China; [b]Department of Chemistry and Chemical Biology, Cornell University, Ithaca, NY 14853; [c]Department of Chemical & Biological Engineering, University of Wisconsin-Madison, Madison, WI 53706; [d]The Institute for Advanced Studies, Wuhan University, Wuhan 430072, China; [e]School of Applied and Engineering Physics, Cornell University, Ithaca, NY 14853; and [f]Kavli Institute at Cornell for Nanoscale Science, Cornell University, Ithaca, NY 14853

Author contributions: Y.G., Y.Y., F.J.D., D.A.M., M.M., L.X., H.D.A., and L.Z. designed research; Y.G., Y.Y., R.S., E.M., H.P., Y.W., C.G., W.J., and G.W. performed research; Y.G. and Y.Y. contributed new reagents/analytic tools; Y.G., Y.Y., R.S., and E.M. analyzed data; Y.G., Y.Y., R.S., and E.M. wrote the paper; and all authors discussed the results and contributed to the final manuscript.

1. I. Staffell *et al.*, The role of hydrogen and fuel cells in the global energy system. *Energy Environ. Sci.* **12**, 463–491 (2019).
2. Y. Yang *et al.*, Octahedral spinel electrocatalysts for alkaline fuel cells. *Proc. Natl. Acad. Sci. U.S.A.* **116**, 24425–24432 (2019).
3. S. Gottesfeld *et al.*, Anion exchange membrane fuel cells: Current status and remaining challenges. *J. Power Sources* **375**, 170–184 (2018).
4. Y. Wang *et al.*, Synergistic Mn-Co catalyst outperforms Pt on high-rate oxygen reduction for alkaline polymer electrolyte fuel cells. *Nat. Commun.* **10**, 1–8 (2019).
5. Y. Xiong, Y. Yang, F. J. DiSalvo, H. D. Abruña, Metal–organic-framework-derived Co–Fe bimetallic oxygen reduction electrocatalysts for alkaline fuel cells. *J. Am. Chem. Soc.* **141**, 10744–10750 (2019).
6. Y. Yang *et al.*, Electrocatalysis in alkaline media and alkaline membrane-based energy technologies. *Chem. Rev.*, 10.1021/acs.chemrev.1c00331 (2022).
7. T. Wang *et al.*, Precious metal-free approach to hydrogen electrocatalysis for energy conversion: From mechanism understanding to catalyst design. *Nano Energy* **42**, 69–89 (2017).
8. E. S. Davydova, S. Mukerjee, J. Frédéric, D. R. Dekel, Electrocatalysts for hydrogen oxidation reaction in alkaline electrolytes. *ACS Catal.* **8**, 6665–6690 (2018).
9. E. S. Davydova, J. Zaffran, K. Dhaka, M. C. Toroker, D. R. Dekel, Hydrogen oxidation on Ni-based electrocatalysts: The effect of metal doping. *Catalysts* **8**, 454–473 (2018).
10. O. V. Cherstiouk *et al.*, Electrocatalysis of the hydrogen oxidation reaction on carbon-supported bimetallic NiCu particles prepared by an improved wet chemical synthesis. *J. Electroanal. Chem. (Lausanne)* **783**, 146–151 (2016).
11. A. Roy *et al.*, Nickel-copper supported on carbon black hydrogen oxidation catalyst integrated into anion-exchange membrane fuel cell. *Sustain. Energy Fuels* **2**, 2268–2275 (2018).
12. W. Sheng *et al.*, Non-precious metal electrocatalysts with high activity for hydrogen oxidation reaction in alkaline electrolytes. *Energy Environ. Sci.* **7**, 1719–1724 (2014).
13. Z. Zhuang *et al.*, Nickel supported on nitrogen-doped carbon nanotubes as hydrogen oxidation reaction catalyst in alkaline electrolyte. *Nat. Commun.* **7**, 1–8 (2016).
14. F. Song *et al.*, Interfacing nickel nitride and nickel boosts both electrocatalytic hydrogen evolution and oxidation reactions. *Nat. Commun.* **9**, 4531–4541 (2018).
15. W. Ni *et al.*, Ni_3N as an active hydrogen oxidation reaction catalyst in alkaline medium. *Angew. Chem. Int. Ed. Engl.* **58**, 7445–7449 (2019).
16. E. S. Davydova, F. D. Speck, M. T. Y. Paul, D. R. Dekel, S. Cherevko, Stability limits of Ni-based hydrogen oxidation electrocatalysts for anion exchange membrane fuel cells. *ACS Catal.* **9**, 6837–6845 (2019).
17. Y. Pan, G. Hu, J. Lu, L. Xiao, L. Zhuang, $Ni(OH)_2$ -Ni/C for hydrogen oxidation reaction in alkaline media. *J. Energy Chem.* **29**, 111–115 (2018).
18. A. G. Oshchepkov, A. Bonnefont, V. N. Parmon, E. R. Savinova, On the effect of temperature and surface oxidation on the kinetics of hydrogen electrode reactions on nickel in alkaline media. *Electrochim. Acta* **269**, 111–118 (2018).
19. Y. Yang *et al.*, Enhanced electrocatalytic hydrogen oxidation on Ni/NiO/C derived from a nickel-based metal-organic framework. *Angew. Chem. Int. Ed. Engl.* **58**, 10644–10649 (2019).
20. A. G. Oshchepkov *et al.*, Nanostructured nickel nanoparticles supported on vulcan carbon as a highly active catalyst for the hydrogen oxidation reaction in alkaline media. *J. Power Sources* **402**, 447–452 (2018).
21. Z. Li *et al.*, Interface-enhanced catalytic selectivity on the C2 products of CO_2 electroreduction. *ACS Catal.* **11**, 2473–2482 (2021).
22. M. Sun *et al.*, Pt@h-BN core–shell fuel cell electrocatalysts with electrocatalysis confined under outer shells. *Nano Res.* **11**, 3490–3498 (2018).
23. M. Karuppannan *et al.*, A highly durable carbon-nanofiber-supported Pt-C core–shell cathode catalyst for ultra-low Pt loading proton exchange membrane fuel cells: Facile carbon encapsulation. *Energy Environ. Sci.* **12**, 2820–2829 (2019).
24. L. Gao *et al.*, A nickel nanocatalyst within a h-BN shell for enhanced hydrogen oxidation reactions. *Chem. Sci. (Camb.)* **8**, 5728–5734 (2017).
25. Y. Goto *et al.*, Formation of Ni_3C nanocrystals by thermolysis of nickel acetylacetonate in oleylamine: Characterization using hard X-ray photoelectron spectroscopy. *Chem. Mater.* **20**, 4156–4160 (2008).
26. K. Chen, S. Zhang, W. Peng, X. Qian, J. Huang, Modification of g-C_3N_4 quantum dots by Ni-Ni_3C@C nanoparticles for hydrogen production. *J. Phys. Chem. Solids* **133**, 100–107 (2019).
27. B. C. Bayer *et al.*, In situ observations of phase transitions in metastable nickel (carbide)/carbon nanocomposites. *J. Phys. Chem. C Nanomater Interfaces* **120**, 22571–22584 (2016).
28. E. Kirkland, *Advanced Computing in Electrons Microscopy* (Springer, New York, 2010).
29. Y. Yang, R. Zeng, Y. Xiong, F. DiSalvo, H. D. Abruña, Rock-salt-type $MnCo_2O_3$/C as efficient oxygen reduction electrocatalysts for alkaline fuel cells. *Chem. Mater.* **31**, 9331–9337 (2019).
30. D. A. Muller, D. J. Singh, J. Silcox, Connections between the electron-energy-loss spectra, the local electronic structure, and the physical properties of a material: A study of nickel aluminum alloys. *Phys. Rev. B Condens. Matter Mater. Phys.* **57**, 8181 (1998).
31. T. Regan *et al.*, Chemical effects at metal/oxide interfaces studied by X-ray-absorption spectroscopy. *Phys. Rev. B Condens. Matter Mater. Phys.* **64**, 214422 (2001).
32. W. Zhao *et al.*, M_xP(M = Co/Ni)@carbon core-shell nanoparticles embedded in 3D cross-linked graphene aerogel derived from seaweed biomass for hydrogen evolution reaction. *Nanoscale* **10**, 9698–9706 (2018).
33. F. Yang *et al.*, Enhanced HOR catalytic activity of PGM-free catalysts in alkaline media: The electronic effect induced by different heteroatom doped carbon supports. *J. Mater. Chem. A Mater. Energy Sustain.* **7**, 10936–10941 (2019).
34. F. Xiao *et al.*, Impact of heat treatment on the electrochemical properties of carbon-supported octahedral Pt-Ni nanoparticles. *ACS Catal.* **9**, 11189–11198 (2019).
35. H. Ren *et al.*, Fe/N/C nanotubes with atomic Fe sites: A highly active cathode catalyst for alkaline polymer electrolyte fuel cells. *ACS Catal.* **7**, 6485–6492 (2017).
36. Y. Yang *et al.*, High-loading composition-tolerant Co–Mn spinel oxides with performance beyond 1 W/cm^2 in alkaline polymer electrolyte fuel cells. *ACS Energy Lett.* **4**, 1251–1257 (2019).
37. D. Banham, S. Ye, Current status and future development of catalyst materials and catalyst layers for proton exchange membrane fuel cells: An industrial perspective. *ACS Energy Lett.* **2**, 629–638 (2017).
38. D. Banham *et al.*, Critical advancements in achieving high power and stable nonprecious metal catalyst-based MEAs for real-world proton exchange membrane fuel cell applications. *Sci. Adv.* **4**, eaar7180 (2018).
39. F. Juarez *et al.*, The initial stage of OH adsorption on Ni(111). *J. Electroanal. Chem. (Lausanne)* **832**, 137–141 (2019).
40. M. Alsabet, M. Grden, G. Jerkiewicz, Electrochemical growth of surface oxides on nickel. Part 1: Formation of α-$Ni(OH)_2$ in relation to the polarization potential, polarization time, and temperature. *Electrocatalysis* **2**, 317–330 (2011).
41. D. S. Hall, C. Bock, B. R. MacDougall, The electrochemistry of metallic nickel: Oxides, hydroxides, hydrides and alkaline hydrogen evolution. *J. Electroanal. Chem. (Lausanne)* **160**, 235–243 (2013).
42. S. Lu, J. Pan, A. Huang, L. Zhuang, J. Lu, Alkaline polymer electrolyte fuel cells completely free from noble metal catalysts. *Proc. Natl. Acad. Sci. U.S.A.* **105**, 20611–20614 (2008).
43. G. Huang *et al.*, Composite poly(norbornene) anion conducting membranes for achieving durability, water management and high power (3.4 W/cm^2) in hydrogen/oxygen alkaline fuel cells. *J. Electroanal. Chem. (Lausanne)* **166**, 637–644 (2019).
44. T. J. Omasta *et al.*, Beyond catalysis and membranes: Visualizing and solving the challenge of electrode water accumulation and flooding in AEMFCs. *Energy Environ. Sci.* **11**, 551–558 (2018).
45. Y. Zheng *et al.*, Quantifying and elucidating the effect of CO_2 on the thermodynamics, kinetics and charge transport of AEMFCs. *Energy Environ. Sci.* **12**, 2806–2819 (2019).
46. J. K. Nørskov *et al.*, Trends in the exchange current for hydrogen evolution. *J. Electrochem. Soc.* **152**, J23 (2005).
47. T. Kropp, M. Mavrikakis, Transition metal atoms embedded in graphene: How nitrogen doping increases CO oxidation activity. *ACS Catal.* **9**, 6864–6868 (2019).
48. T. Kropp, M. Rebarchik, M. Mavrikakis, On the active site for electrocatalytic water splitting on late transition metals embedded in graphene. *Catal. Sci. Technol.* **9**, 6793–6799 (2019).